Journal of Materials Chemistry C

ROYAL SOCIETY OF CHEMISTRY

PAPER

View Article Online
View Journal | View Issue

Check for updates

Cite this: J. Mater. Chem. C, 2025, 13, 5582

Efficient and low roll-off solution-processed sky-blue TADF emitters *via* hetero-donor and space modification strategies†

Hao-Nan Shi,[a] Feng-Ming Xie,*[a] Hao-Ze Li,[b] Yan-Qing Li*[b] and Jian-Xin Tang*[ac]

Received 18th December 2024,
Accepted 22nd January 2025

DOI: 10.1039/d4tc05347h

rsc.li/materials-c

Solution-processed thermally activated delayed fluorescence (TADF) organic light-emitting diodes (OLEDs) have traditionally underperformed compared to vacuum-deposited OLEDs, primarily due to low external quantum efficiency (EQE) and severe efficiency roll-off at high brightness. Herein, a strategic molecular design for solution-processable TADF emitters featuring multiple-donor shielded lowest unoccupied molecular orbital (LUMO) structures is proposed by filling rigid bulky phenyl substituents (monophenyl, diphenyl and *m*-triphenyl) into a hetero-donor TADF core. The introduced bulky units not only effectively suppress the aggregation-caused quenching (ACQ) effect in the solid state, but also accelerate the up-conversion process. The corresponding solution-processed TADF-OLEDs exhibit a maximum external quantum efficiency (EQE_{max}) exceeding 20% and low efficiency roll-off. Among them, the HCB-3-based device demonstrates the highest performance, with an EQE of 24.1% and maintaining 23.7% at 100 cd m^{-2}. These results highlight the significant potential for developing high-efficiency and low roll-off solution-processed TADF materials, representing a promising advancement in OLED technology.

1. Introduction

As the importance and advantages of thermally activated delayed fluorescence organic light-emitting diodes (TADF-OLEDs) gain recognition, their potential applications in solid-state lighting and displays are being thoroughly explored. In recent years, research has concentrated on developing high-performance TADF emitters that can be processed in solution.[1–6] These emitters exhibit a small energy splitting (ΔE_{ST}) between the excited singlet and triplet states, which promotes reverse intersystem crossing (RISC). The process converts triplet excitons to singlet states, allowing TADF materials to harvest both singlet and triplet excitons, thereby achieving an internal quantum efficiency (IQE) of up to 100%.[7,8] Currently, most TADF devices are produced using the traditional vacuum evaporation process, which faces significant challenges, such as substantial material loss and poor control of low doping concentrations.[9–13] As an alternative, solution-processed OLEDs offer several advantages, including low-cost manufacturing, efficient material usage, precise doping concentration control, and scalability.[14–20] However, solution-processed OLEDs generally underperform compared to vacuum-deposited devices in terms of external quantum efficiency (EQE) and device stability. Consequently, the development of economical solution-processed OLEDs based on TADF materials is the primary focus of both academic and industrial research.

Efficient blue TADF emitters typically require a combination of weak intramolecular charge transfer effects, enhanced molecular rigidity, and minimal spatial overlap between the highest occupied molecular orbital (HOMO) and the lowest unoccupied molecular orbital (LUMO).[21–24] However, during the film formation process, solution processable blue TADF inks often suffer from aggregation and phase separation, leading to aggregation-caused quenching (ACQ) and a sharp drop in performance.[25–28] To address this crucial drawback, researchers are exploring the use of bulky molecules with large steric hindrances, which can form stable amorphous films through solution processing.[29–31] These stereoscopic and bulky molecular frameworks also increase intermolecular distances, reducing

[a] Jiangsu Key Laboratory for Carbon-Based Functional Materials & Devices, Institute of Functional Nano & Soft Materials (FUNSOM), Soochow University, Suzhou, Jiangsu, 215123, P. R. China. E-mail: fmxie@suda.edu.cn
[b] School of Physics and Electronic Science, Ministry of Education Nanophotonics & Advanced Instrument Engineering Research Center, East China Normal University, Shanghai, 200062, P. R. China. E-mail: yqli@phy.ecnu.edu.cn
[c] Macao Institute of Materials Science and Engineering (MIMSE), Faculty of Innovation Engineering, Macau University of Science and Technology, Taipa, Macao, 999078, P. R. China. E-mail: jxtang@must.edu.mo

† Electronic supplementary information (ESI) available. See DOI: https://doi.org/10.1039/d4tc05347h

host–dopant/dopant–dopant interactions and mitigating exciton quenching effects, ultimately improving device efficiency.[30,32–35] Several molecular strategies have proved successful in achieving an EQE of more than 20% for solution-processed TADF-OLEDs, such as the incorporation of rigid spiro segments,[36] the creation of dendritic molecular structures,[30,37] and the utilization of hyperfluorescent systems.[38,39] Despite these advancements, most solution-processed TADF-OLEDs cause a serious efficiency roll-off due to the lower RISC rate, with EQE_{1000} (EQE at 1000 cd m^{-2}) below 10%,[40–46] which is considerably inferior to that of the vacuum-deposited counterparts. Therefore, developing solution-processed TADF emitters that are resistant to efficiency roll-off remains highly desirable.

In this study, we designed three solution processable blue TADF emitters with hetero-carbazole donors and benzonitrile acceptors, namely HCB-1, HCB-2, and HCB-3. Carbazole units were chosen for their excellent hole conductivity, amorphous properties, and robust thermal and morphological stability.[12,47,48] Additionally, we used 3,6-di-*tert*-butylcarbazole as a secondary donor unit to achieve a small ΔE_{ST} and high photoluminescent quantum yield (PLQY).[49] The *tert*-butyl groups enhanced molecular solubility and reduce aggregation-caused quenching (ACQ) by inhibiting intermolecular π–π stacking.[50] Benzonitrile as the acceptor unit could reduce the triple energy level and enhance the chemical stability of materials. The combination of cyano groups with carbazole units results in promising TADF emitters for high-efficiency devices.[51,52] To further prevent molecular aggregation in the film,[39] rigid bulky phenyl derivatives (monophenyl, diphenyl, and *m*-triphenyl) were introduced as *para*-substituents for the cyano group (Fig. 1). The three target molecules exhibit small ΔE_{ST}, high PLQY and fast k_{RISC}. Using solution-processed OLEDs based on these dopants sky-blue emission in the range of 486 to 496 nm was achieved, with an EQE exceeding 20% and low efficiency roll-off at high brightness. Among them, HCB-3 demonstrates the highest EQE of 24.1% and minimal efficiency roll-off at high brightness (EQE_{100} = 23.7% and EQE_{1000} = 15.2%) compared to HCB-1 and HCB-2. These results open new avenues for the development of highly efficient and low roll-off solution-processable TADF-OLEDs.

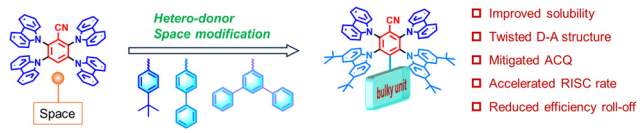

Fig. 1 Molecular design strategies for three materials.

2. Results and discussion

2.1 Synthesis and characterization

The synthesis and characterization of HCB-1, HCB-2, and HCB-3 are detailed in Schemes S1–S3 and Fig. S1–S9, ESI.† The benzonitrile moiety was chosen as the acceptor, while carbazole and *tert*-butyl carbazole acted as donors. The addition of para-substituted phenyl derivatives of the cyano group enhanced the donor–acceptor (D–A) distortion, resulting in a three-dimensional stereochemical configuration. All three emitters exhibited desirable solubility in common solvents such as CH_2Cl_2, dimethylformamide (DMF) and toluene. Furthermore, thermogravimetric analysis (TGA), as shown in Fig. S10, ESI,† indicated that the emitters possess good thermal stability. The decomposition temperatures (T_d, at 5% weight loss) were determined to be 415 °C, 454 °C, and 480 °C for HCB-1, HCB-2, and HCB-3, respectively (Table 1).

2.2 Single crystals

Single crystals of HCB-1 and HCB-2 were grown by slow volatilization of a mixed CH_2Cl_2/CH_3CH_2OH solution at room temperature, and single crystals of HCB-3 were obtained using a temperature-gradient vacuum sublimation technique (Fig. S11 and Tables S1–S3, ESI†). X-ray crystallography analysis revealed a highly twisted donor shielding acceptor structure, with significant torsion angles between carbazole/*tert*-butyl carbazole and benzonitrile (Fig. 2a). In HCB-1, the dihedral angles of the four carbon–nitrogen single bonds (donor–acceptor bonds) range from 62° to 72°. When the *tert*-butylbenzene ring is substituted by biphenyl or *m*-terphenyl, the dihedral angles increase. Sequentially, HCB-2 exhibits dihedral angles of 65° to 75°, and HCB-3 shows dihedral angles of 75° to 87°. These results indicate that substituents with large steric hindrance positively impact the stereospecificity of non-rigid conjugated systems. The HCB derivatives are anticipated to have a small ΔE_{ST} value owing to their pre-twisted D–A skeleton. As shown in Fig. 2b, the inter-plane distance between two adjacent carbazole moieties increases from 3.219 Å in HCB-1 to 3.566 Å in HCB-2 and 3.579 Å in HCB-3. Moreover, the planar spacing between two neighboring benzonitrile molecules is 9.873 Å in HCB-2 and 10.839 Å in HCB-3. The multiple donor shielding of the LUMO structure suggests that LUMO–LUMO overlap is effectively restricted. These findings indicate that the bulky phenyl substituents effectively prevent intermolecular π–π stacking interactions, thereby reducing ACQ effects in the aggregated state.

Table 1 Summary of key physical parameters of HCB-1, HCB-2, and HCB-3

Compound	λ_{abs} [a] (nm)	PL [b] (nm)	S_1 [c] (eV)	T_1 [c] (eV)	ΔE_{ST} [d] (eV)	τ_p/τ_d [e] (ns/μs)	Φ_{PL} [f] (%)	HOMO [g] (eV)	LUMO [g] (eV)	T_d [h] (°C)
HCB-1	413	465	2.74	2.73	0.01	35.24/15.23	81/73	−5.65	−2.65	415
HCB-2	418	472	2.81	2.75	0.06	29.43/57.83	85/76	−5.66	−2.70	464
HCB-3	411	472	2.74	2.71	0.03	41.43/8.71	92/83	−5.67	−2.66	448

[a] Measured in dilute toluene at room temperature. [b] Measured in dilute toluene at room temperature. [c] Calculated from the onset wavelength of the fluorescence and phosphorescence spectra, respectively. [d] $\Delta E_{ST} = S_1 - T_1$. [e] Prompt and delayed lifetimes of doped films. [f] Absolute Φ_{PL} of doped films and in toluene (10^{-5} M) measured using an integrating sphere under a nitrogen atmosphere. [g] Determined by cyclic voltammetry curves and E_g. [h] 5% weight loss determined from TGA curves.

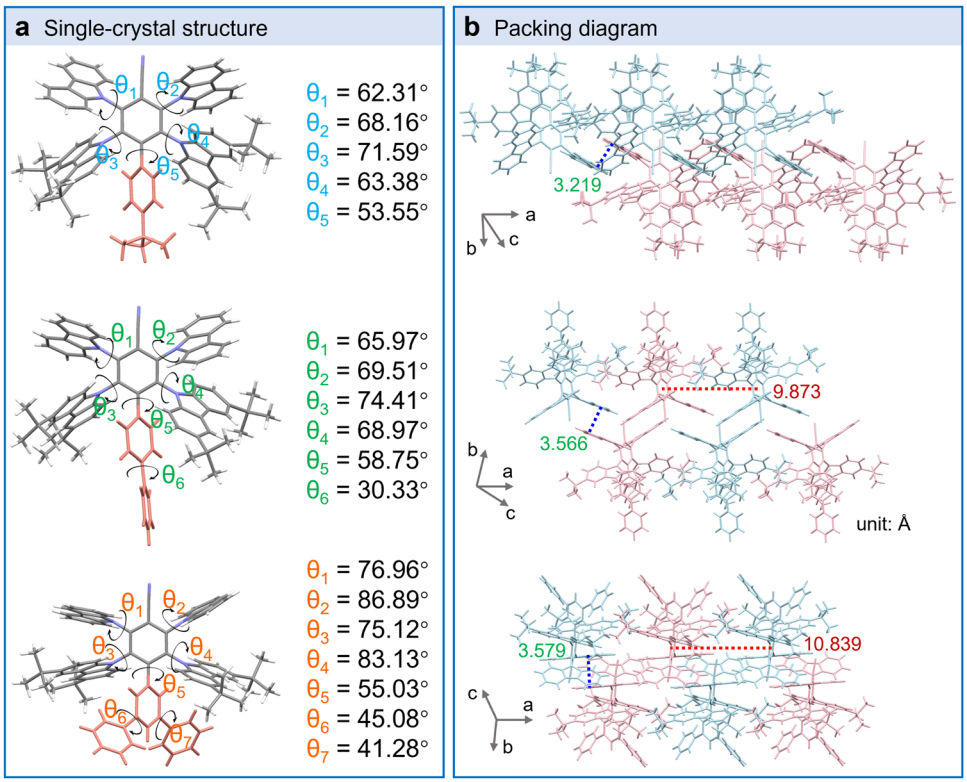

Fig. 2 (a) Side and top views of the single-crystal structure and (b) packing analysis of HCB-1, HCB-2, and HCB-3 (unit: Å).

2.3 Theoretical calculations

To examine the influence of integrating multiple units on the optimized molecular structure and the distribution of frontier molecular orbitals (FMOs), the electron cloud distributions of HCB-1, HCB-2, and HCB-3 were calculated using density functional theory (DFT) and time-dependent DFT (TD-DFT) using the B3LYP/6-31G(d) method. As shown in Fig. 3, the optimized geometries of these molecules reveal that their distorted D–A structures effectively suppress the spatial overlap between the HOMO and the LUMO. Apparently, the HOMO is mainly located on the donor unit, while the LUMO is distributed not only on the benzonitrile acceptor but also extends toward the cyano-para-phenyl substituent, mainly to the first benzene ring. The distribution, shielded by multiple donors and bulky substituents, mitigates the short-range Dexter energy transfer (DET) process.[53] Due to identical donor and acceptor segments as well as similar FMOs, the three emitters exhibit similar HOMO and LUMO energy levels. The calculated HOMO and LUMO energy levels are 5.29 and 1.96 eV for HCB-1, 5.32 and 2.01 eV for HCB-2, and 5.32 and 1.67 eV for HCB-3, respectively. Consequently, the band gaps are calculated to be 3.33 eV for HCB-1, 3.31 eV for HCB-2, and 3.35 eV for HCB-3, which are favorable for achieving a blue emission. Furthermore, the analysis of natural transition orbitals (NTOs) indicates that T_2 for HCB-1, T_1 for HCB-2, and T_2 for HCB-3 possess hybridized local and charge-transfer (HLCT) properties due to some overlap of holes and electrons (Fig. S12–S14, ESI†). To obtain additional insights into the spin–flip RISC process, the spin–orbit coupling (SOC) for the S_1 and T_n (≤ 3) states of HCB-1, HCB-2, and HCB-3 were calculated (Fig. S15, ESI†). For HCB-1, the significant difference in the excitation characteristics between the S_1 and T_1 states results in a high SOC value of 0.542 cm^{-1}. As the size of the phenyl ring substituents increases sequentially, the electronic configurations of the T_2 state in HCB-2 and HCB-3 become markedly different from that of the S_1 state, leading to high SOC values of 0.621 cm^{-1} and 0.826 cm^{-1}, respectively. The larger SOC value for the T_2–S_1 transition in HCB-3 indicates its potential for a rapid RISC process. The calculated S_1/T_1 excitation energies are 2.114/2.016 eV for HCB-1, 2.216/2.200 eV for HCB-2, and 2.070/2.014 eV for HCB-3. The corresponding ΔE_{ST} values are 0.053, 0.016, and 0.056 eV for HCB-1, HCB-2, and HCB-3, respectively. These small ΔE_{ST} values facilitate the RISC process, essential for highly efficient and low roll-off TADF emitters.

2.4 Electrochemical properties

Cyclic voltammetry (CV) measurements were carried out to understand the electrochemical properties of the three synthesized materials (Fig. S16, ESI†). The HOMO energy levels were obtained from the oxidation potential. The reduction reaction process of organic molecules is complicated. And because the band gap value measured by cyclic voltammetry exhibits a large difference with the optical measurement value, we adopt the

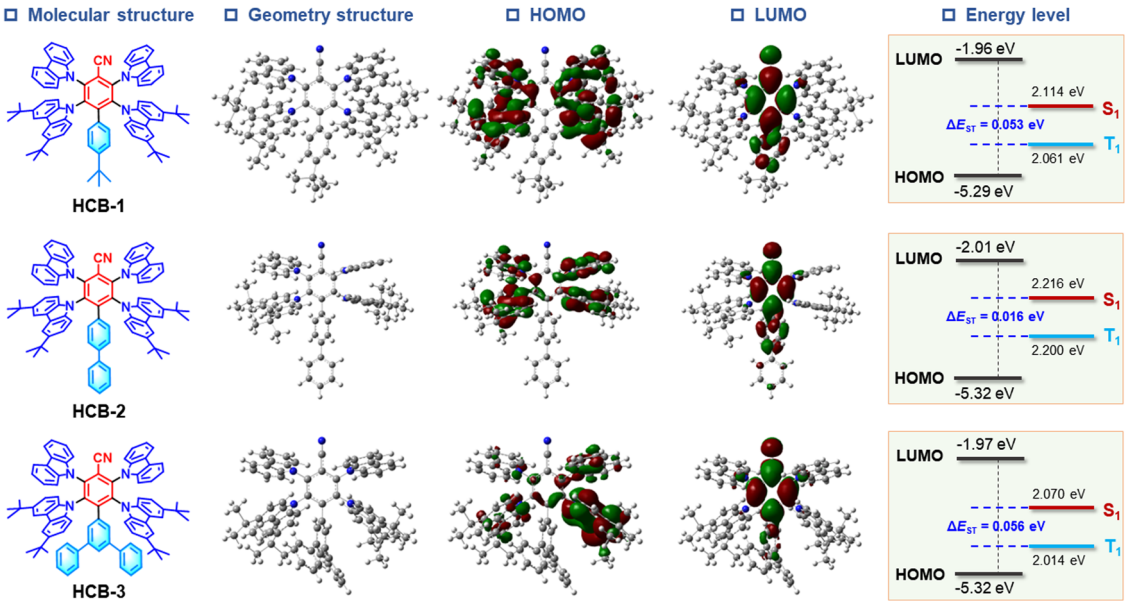

Fig. 3 The molecular structure, geometry structure, and HOMO, LUMO and energy levels of three compounds.

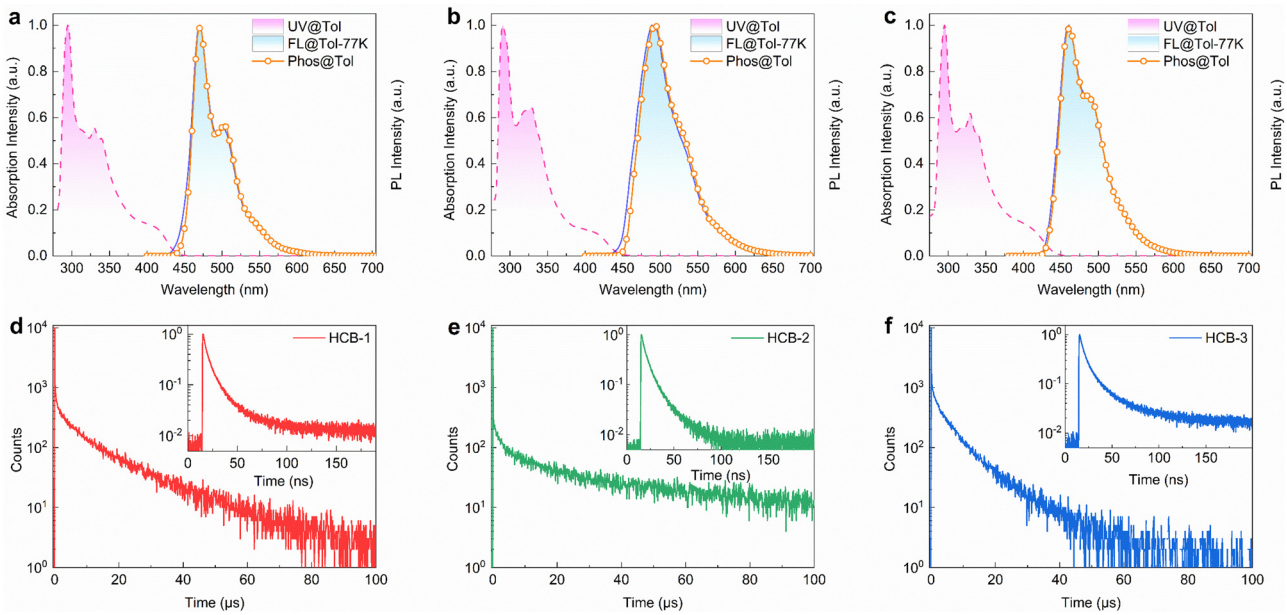

Fig. 4 Normalized absorption, phosphorescence and PL spectra of (a) HCB-1, (b) HCB-2, and (c) HCB-3 measured in toluene (10^{-5} M) at 77 K. Transient PL decay curves of (d) HCB-1, (e) HCB-2, and (f) HCB-3 measured in doped films (20 wt% spin-coated film doped in mCP host) under vacuum conditions at RT.

method of combining cyclic voltammetry and optical bandgap (E_g) to indirectly deduce the LUMO energy level of organic molecules. The HOMO/LUMO energy levels are 5.65/2.65 eV for HCB-1, 5.66/2.70 eV for HCB-2, and 5.67/2.66 eV for HCB-3, respectively.

2.5 Photophysical properties

To investigate the photophysical properties of HCB-1, HCB-2, and HCB-3, the ultraviolet-visible (UV-vis) absorption and photoluminescence (PL) spectra were measured in dilute toluene solution (Fig. 4a–c). The UV-vis absorption spectra revealed that all three compounds exhibit similar absorption properties. The strong absorption bands at 280–370 nm are attributed to the π–π* and n–π* transitions in the donor unit of carbazole derivatives, while the lower absorption peak near 410 nm originates from intramolecular charge transfer (ICT) from multiple donors to the acceptor core. The fluorescence spectra (FL) of HCB-1, HCB-2 and HCB-3 in toluene solutions at room-temperature showed blue emission peaks at 465, 472 and 472 nm and in 100 wt% films at room temperature showed

sky blue emission peaks at 485, 492 and 492 nm, respectively (Fig. S17 and S18, ESI†). The PL spectra in 100 wt% films show a slight redshift compared with that in solutions due to the effect of the intermolecular forces and the aggregation state. The S_1 and T_1 energy levels were determined from the onset emission wavelengths of the low-temperature FL and low-temperature phosphorescence (Phos) spectra under liquid nitrogen. The corresponding ΔE_{ST} values were estimated to be 0.01, 0.06, and 0.03 eV for HCB-1, HCB-2 and HCB-3, respectively. These small ΔE_{ST} values facilitate the RISC process to utilize the dark triplet state excitons, indicating efficient TADF properties. The key photophysical parameters are summarized in Table 1.

Additionally, the PL spectra of these emitters in solvents with different solvent polarities were measured. As shown in Fig. S20, ESI,† all three emitters exhibit significant solvatochromic effects with the PL spectra red-shifting and broadening as solvent polarity increases. The emission peaks of HCB-1, HCB-2, and HCB-3 red-shifted by 59, 53, and 52 nm from nonpolar *n*-hexane to polar dichloromethane, respectively, suggesting ICT properties in the excited state. Moreover, the PL spectra of HCB-1, HCB-2, and HCB-3 in THF/H_2O mixtures with varying water fractions were also observed to study excited state radiation dynamics in the aggregated state, illustrating the obvious aggregation-induced emission-enhanced (AIEE) properties (Fig. S21, ESI†). HCB-1, HCB-2, and HCB-3 exhibited maximum emission intensities at weight fractions (f_w) of 50%, 50%, and 60%, respectively (Fig. S21, ESI†). This indicates that the ACQ of these materials under highly aggregated conditions is effectively suppressed, thus enabling them to exhibit excellent luminescent properties.

To study the TADF properties of HCB-1, HCB-2, and HCB-3, transient PL (TRPL) spectra of the emitters doped in the mCP host were measured at 300 K (Fig. 4d–f). The TRPL signals of HCB-1, HCB-2, and HCB-3 all exhibited nanosecond-scale prompt fluorescence (τ_p) and microsecond-scale delayed fluorescence (τ_d) components, indicating excellent TADF properties for these emitters. The τ_p/τ_d values of HCB-1, HCB-2, and HCB-3 were determined to be 35.24 ns/15.23 μs, 29.43 ns/57.83 μs, and 41.43 ns/8.71 μs, respectively. These three materials exhibit very small S_1–T_1 energy differences. However, the measured delayed fluorescence lifetimes span a relatively wide range (8.71–57.83 μs). The RISC rates of HCB-1 and HCB-2 are relatively smaller compared to HCB-3, leading to a certain amount of time required for the conversion of triplet excitons to singlet excitons.[54] This slow RISC process may contribute to the prolonged delayed fluorescence lifetimes. Furthermore, the radiative transition process from the S_1 state to the ground state (S_0) is a crucial step in the production of delayed fluorescence. In this process, singlet excitons return to the ground state by emitting photons. The speed of the radiative transition rate directly affects the lifetime of delayed fluorescence. The longer delayed fluorescence lifetimes of HCB-1 and HCB-2 result in slower RISC rates.[55] The doped/nondoped films of HCB-1, HCB-2 and HCB-3 were fabricated to assess the PLQY. As depicted in Fig S22, ESI,† within a certain range, PLQY increases with increasing concentration, indicating that the steric hindrance effect of the multiple-donor shielding structure effectively hinders molecular aggregation, thereby reducing ACQ.[56] The PLQY values of HCB-1, HCB-2, and HCB-3 doped films and in toluene were found to be 81%, 85%, and 92% and 73%, 76%, and 83%, respectively. Due to the weakened ACQ effect, the arrangement of materials in thin films is tighter compared to that in solutions. This compact molecular arrangement facilitates exciton transfer and radiative transitions, thus enhancing PLQY. Kinetic parameters such as the radiative decay rate constant from the singlet excited state (k_r), the non-radiative decay rate constant from the singlet excited state (k_{nr}), the intersystem crossing (ISC) rate constant (k_{ISC}), and RISC rate constant (k_{RISC}) were calculated from the lifetimes and PLQY using the reported method (Table S4, ESI†).[26,57] Short delayed lifetimes give rise to fast RISC processes, which are important for efficient triple state exciton utilization and reduction of non-radiative processes. As shown in Table S4, k_r, k_{nr}, and k_{RISC} have been calculated, and all three materials exhibit fast k_r values on the order of 10^7. Moreover, HCB-3 has the largest k_{RISC} and the smallest k_{nr}, indicating its excellent exciton utilization efficiency and predictable low-efficiency roll-off. Furthermore, temperature-dependent TRPL curves were measured in doped films from 100 K to 300 K. The relative intensity of the delay component increased with temperature as shown in Fig. S24, ESI.† As the temperature increases, the k_{RISC} of HCB-3 increases the fastest and remains the highest, suggesting that HCB-3 has more excitons transitioning from the triplet state to the singlet state (Fig. S25, ESI†). Furthermore, its shorter delayed lifetime indicates that HCB-3 can minimize triplet–triplet annihilation (TTA).[58] These features are consistent with the nature of the TADF emission, suggesting that exciton transition occurs from T_1 to S_1 *via* the RISC process and then to the S_0.

To gain further insight into the photophysical properties of HCB-1, HCB-2 and HCB-3 in the film state, solution-processed doped films were prepared at 20 wt% doped concentrations using mCP as the host matrix. The film-forming properties of HCB-1, HCB-2 and HCB-3 were evaluated through atomic force microscopy (AFM) analyses in a 20 wt% doped film. The results showcased exceptional morphological stability, as evidenced by a small root-mean-square (RMS) values of 0.373, 0.379 and 0.376 nm (Fig. S26, ESI†), indicating excellent film-forming quality and superior solution processing properties.

2.6 Device performances

The electroluminescence (EL) performance of the three emitters were further investigated by the fabrication of solution-processed OLEDs using HCB-1, HCB-2, and HCB-3 as dopants. The devices were prepared with the following configurations: ITO/PEDOT:PSS (40 nm)/PVK (10 nm)/mCP:*x* wt% emitters (30 nm, *x* = 10, 20, 30, and 100)/DPEPO (10 nm)/TmPyPB (40 nm)/LiF (1 nm)/Al (100 nm). Here, PEDOT:PSS is used for the hole injection and transport layer, while the TmPyPB and DPEPO serve as electron transport layer and hole blocking layer, respectively. The omission of PVK leads to reduced efficiency and increased efficiency roll-off, which indicates significant exciton loss and subsequently poorer device performance.

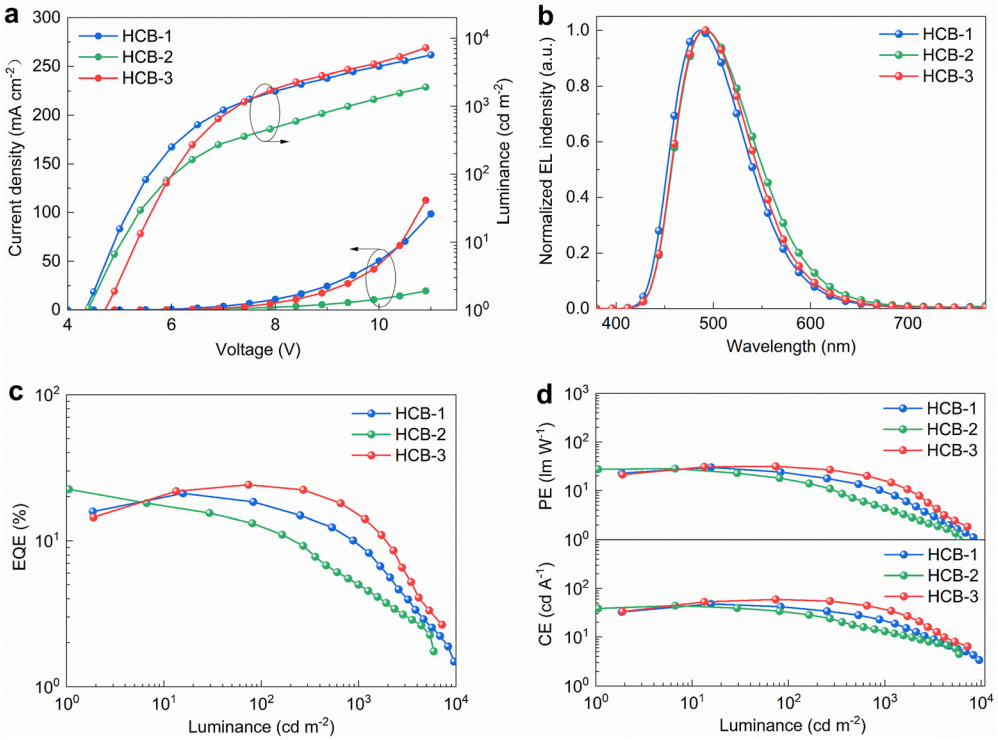

Fig. 5 (a) Current density and luminance *versus* voltage (*J*–*V*–*L*) characteristics. (b) EL spectra at a luminance of 1000 cd m^{-2}. (c) EQE as a function of luminance. (d) PE and CE as a function of luminance.

Therefore, PVK serves as an electron and exciton-blocking layer. (Fig. S27, ESI†). Due to the higher efficiency and smaller efficiency roll-off, the TADF emitters doped in the mCP host as an emitting layer (EML) (Fig. S28, ESI†) The device structure, energy level diagram, and the molecular structure of the functional layer materials are displayed in Fig. S29, ESI.† Optimal device performances are shown in Fig. 5 and related EL parameters are summarized in Table 2. Other device performances with different doping concentrations are presented in Fig. S30–S32 and Tables S6–S8, ESI.† HCB-1-, HCB-2-, and HCB-3-based devices exhibited sky-blue emission with maximum EL peaks at 486 nm, 496 nm and 492 nm, respectively (Fig. 5c). Moreover, as the voltage increases, the emission peaks and CIE coordinates of these three materials exhibit nearly no variation, indicating their excellent spectral stability (Fig. S33 and S34, ESI†). The PL of HCB-1, HCB-2, and HCB-3 in doped films exhibited blue emission peaks at 481 nm, 481 nm, and 487 nm, respectively, at room temperature (Fig. S19, ESI†). The red-shift of EL emission compared to PL emission indicates the influence of various functional layers, including the host material. The type of material, thickness, and energy band structure of these layers all have an impact on the luminescent properties of the luminescent material. In particular, when the luminescent material is subjected to an electric field, its energy level structure and electron distribution may undergo changes, leading to differences in the position of the EL peak compared to the PL peak.[59] The HCB-1- and HCB-2-based TADF-OLEDs achieved EQE_{max} of 21.0% and 22.4%, respectively. The solution-processed device employing HCB-3 demonstrated an EQE_{max} value of up to 24.1%, remaining high at 23.7% at 100 cd m^{-2} and 15.2% at 1000 cd m^{-2}. This low efficiency roll-off is attributed to shorter delayed lifetime and faster k_{RISC} rate, effectively reducing the TTA and triplet-polaron annihilation (TPA) processes.[60] To understand the fundamental physical principles governing the efficiency roll-off behavior, the transient EL decay curves of devices HCB-1, HCB-2, and HCB-3 under different voltages were examined, as shown in Fig. S35, ESI.† As the voltage increased, the period during which carriers

Table 2 OLED performance based on HCB-1, HCB-2, and HCB-3

EML	V_{on}[a] (V)	EQE[b] (%)	$EQE_{roll\text{-}off}$[c] (%)	CE[d] (cd A^{-1})	PE[d] (lm W^{-1})	λ_{EL}[e] (nm)	FWHM[e] (nm)	CIE[e] (x, y)
HCB-1	4.3	21.0/17.6/9.4	16.1/55.2	48.1	30.2	486	85	(0.18, 0.36)
HCB-2	4.4	22.4/12.4/5.0	44.6/77.6	44.2	28.3	496	92	(0.23, 0.39)
HCB-3	4.7	24.1/23.7/15.2	0.1/36.9	59.4	31.6	492	87	(0.19, 0.39)

[a] Turn-on voltage. [b] Maximum EQE, and values at 100 and 1000 cd m^{-2}. [c] $EQE_{roll\text{-}off} = (EQE_{max} - EQE_{100/1000})/EQE_{max}$. [d] Maximum CE and PE. [e] EL peak, FWHM and CIE color coordinates.

injected from the electrodes into the EML and the duration from the initiation of the EL response to the saturation of EL intensity gradually shortened. Furthermore, compared to HCB-1 and HCB-2, HCB-3 exhibited shorter onset and rise times, indicating its higher carrier mobility. Additionally, the faster decay rate of HCB-3 suggests its smaller efficiency roll-off.[61] The impedance of devices HCB-1, HCB-2, and HCB-3 were measured. (Fig. S36, ESI†). From the plots, as the impedance of devices HCB-1, HCB-2, and HCB-3 decreases sequentially, the HCB-3 possesses better charge injection and transport properties, leading to faster device response speed.[62] The operational stabilities of these devices were measured at an initial luminance of 100 cd m^{-2} (Fig. S37, ESI†). The HCB-1, HCB-2, and HCB-3-based devices exhibited LT_{50} of 22.4 h, 4.0 h, and 24.0 h. Under the influence of electric fields and optical radiation, the chemical bonds in OLED materials may undergo breakage, leading to the destruction of molecular structures. This destruction can trigger a series of chain reactions, further accelerating the degradation of the materials. Meanwhile, the broken chemical bonds may also recombine to form new molecular structures, but these new structures often impair the luminescent properties. Additionally, in OLED devices, the transport of holes and electrons needs to be balanced to ensure the effective formation of excitons in the guest material. If the charge transport properties of the host material are poor, it will lead to the accumulation of charges at the interface, subsequently causing issues such as charge injection barriers and exciton quenching. These problems all degrade the luminescence efficiency and stability of the devices.[63] Although its performance is inferior to that of the reported optimal vacuum evaporation equipment, this strategy effectively addresses the efficiency roll-off issue of solution-processed devices at high brightness (Table S10, ESI†). Among these blue-emitting devices, the HCB-3-based device performs the best, surpassing most reported solution-processed TADF OLEDs in terms of efficiency roll-off (Table S9, ESI†).[40,44,64–71] In addition, non-doped solution-processed devices using these three TADF materials as the EML exhibited favorable EQE_{max} values of 12–15% (Fig. S30–S32, ESI†). The biggest advantage of solution-processed devices is that they are easier to prepare for large-area applications and have lower costs. These advantages make solution processing a promising candidate for wide application and important research value in the field of optoelectronics as well as other related fields.[72–74]

3. Conclusions

In summary, we proposed a strategic design for solution-processable TADF emitters using multiple hetero-donor shielded LUMO and space-filling approaches. The hetero-donor system effectively mixes charge transfer and locally excited triplet states. The steric effect of rigid bulky phenyl derivatives and *tert*-butyl groups significantly mitigates intermolecular π–π stacking interactions and suppresses ACQ, resulting in an accelerated RISC rate and high PLQY in the solid state. Solution-processed OLEDs using these sky-blue emitters achieved an EQE value of over 20% with low efficiency roll-off. Notably, the HCB-3-based device demonstrated superior performance with a maximum EQE value of as high as 24.1%, maintaining 23.7% at 100 cd m^{-2} and 15.2% at 1000 cd m^{-2}, which is outstanding among reported solution-processed TADF-OLEDs. This molecular design strategy is useful for enhancing the performance of solution-processed TADF emitters and reducing device efficiency roll-off.

Data availability

The data that support the findings of this study are available on request from the corresponding author upon reasonable request.

Conflicts of interest

There are no conflicts to declare.

Acknowledgements

The authors acknowledge financial support from the National Key R&D Program of China (No. 2022YFE0206100), the Science and Technology Development Fund (FDCT), Macao SAR (No. 0008/2022/AMJ), the National Natural Science Foundation of China (No. U23A20371 and 52303244), the Jiangsu Provincial Department of Science and Technology (No. BZ2022054), the Bureau of Science and Technology of Suzhou Municipality (No. SYC2022144), the Guangdong Science and Technology Plan (No. 2023A0505030015), and the Collaborative Innovation Center of Suzhou Nano Science & Technology.

Notes and references

1 Y. Chen, D. Zhang, Y. Zhang, X. Zeng, T. Huang, Z. Liu, G. Li and L. Duan, *Adv. Mater.*, 2021, **33**, 2103293.
2 T.-H. Han, M.-R. Choi, C.-W. Jeon, Y.-H. Kim, S.-K. Kwon and T.-W. Lee, *Sci. Adv.*, 2016, **2**, e1601428.
3 G. Hong, X. Gan, C. Leonhardt, Z. Zhang, J. Seibert, J. M. Busch and S. Bräse, *Adv. Mater.*, 2021, **33**, 2005630.
4 Y. X. Hu, J. Miao, T. Hua, Z. Huang, Y. Qi, Y. Zou, Y. Qiu, H. Xia, H. Liu, X. Cao and C. Yang, *Nat. Photonics*, 2022, **16**, 803–810.
5 W. Zhu and K. B. Crozier, *Nat. Commun.*, 2014, **5**, 5228.
6 Q. Zhang, H. Kuwabara, W. J. Potscavage, Jr., S. Huang, Y. Hatae, T. Shibata and C. Adachi, *J. Am. Chem. Soc.*, 2014, **136**, 18070–18081.
7 H. Uoyama, K. Goushi, K. Shizu, H. Nomura and C. Adachi, *Nature*, 2012, **492**, 234–238.
8 N. Aizawa, Y.-J. Pu, M. Watanabe, T. Chiba, K. Ideta, N. Toyota, M. Igarashi, Y. Suzuri, H. Sasabe and J. Kido, *Nat. Commun.*, 2014, **5**, 5756.
9 L. Duan, L. Hou, T.-W. Lee, J. Qiao, D. Zhang, G. Dong, L. Wang and Y. Qiu, *J. Mater. Chem.*, 2010, **20**, 6392–6407.

10 C. D. Müller, A. Falcou, N. Reckefuss, M. Rojahn, V. Wiederhirn, P. Rudati, H. Frohne, O. Nuyken, H. Becker and K. Meerholz, *Nature*, 2003, **421**, 829–833.
11 K. S. Yook and J. Y. Lee, *Adv. Mater.*, 2014, **26**, 4218–4233.
12 C. Zhong, C. Duan, F. Huang, H. Wu and Y. Cao, *Chem. Mater.*, 2011, **23**, 326–340.
13 J. Hwang, H. Kang, J.-E. Jeong, H. Y. Woo, M. J. Cho, S. Park and D. H. Choi, *Chem. Eng. J.*, 2021, **416**, 129185.
14 N. Ikeda, S. Oda, R. Matsumoto, M. Yoshioka, D. Fukushima, K. Yoshiura, N. Yasuda and T. Hatakeyama, *Adv. Mater.*, 2020, **32**, 2004072.
15 K. Kishore Kesavan, J. Jayakumar, M. Lee, C. Hexin, S. Sudheendran Swayamprabha, D. Kumar Dubey, F.-C. Tung, C.-W. Wang and J.-H. Jou, *Chem. Eng. J.*, 2022, **435**, 134879.
16 B. Li, Z. Yang, W. Gong, X. Chen, D. W. Bruce, S. Wang, H. Ma, Y. Liu, W. Zhu, Z. Chi and Y. Wang, *Adv. Opt. Mater.*, 2021, **9**, 2100180.
17 Y. Liu, L. Hua, Z. Zhao, S. Ying, Z. Ren and S. Yan, *Adv. Sci.*, 2021, **8**, 2101326.
18 W. Zeng, T. Zhou, W. Ning, C. Zhong, J. He, S. Gong, G. Xie and C. Yang, *Adv. Mater.*, 2019, **31**, 1901404.
19 J. Zhang, Y. Wei and H. Xu, *Nano Energy*, 2021, **83**, 105746.
20 D. H. Ahn, S. W. Kim, H. Lee, I. J. Ko, D. Karthik, J. Y. Lee and J. H. Kwon, *Nat. Photonics*, 2019, **13**, 540–546.
21 Y. Im, M. Kim, Y. J. Cho, J.-A. Seo, K. S. Yook and J. Y. Lee, *Chem. Mater.*, 2017, **29**, 1946–1963.
22 W. Li, M. Li, W. Li, Z. Xu, L. Gan, K. Liu, N. Zheng, C. Ning, D. Chen, Y.-C. Wu and S.-J. Su, *ACS Appl. Mater. Interfaces*, 2021, **13**, 5302–5311.
23 Z. Yang, Z. Mao, Z. Xie, Y. Zhang, S. Liu, J. Zhao, J. Xu, Z. Chi and M. P. Aldred, *Chem. Soc. Rev.*, 2017, **46**, 915–1016.
24 W. Li, B. Li, X. Cai, L. Gan, Z. Xu, W. Li, K. Liu, D. Chen and S.-J. Su, *Angew. Chem., Int. Ed.*, 2019, **58**, 11301–11305.
25 G. Chen, J. Wang, W.-C. Chen, Y. Gong, N. Zhuang, H. Liang, L. Xing, Y. Liu, S. Ji, H.-L. Zhang, Z. Zhao, Y. Huo and B. Z. Tang, *Adv. Funct. Mater.*, 2023, **33**, 2211893.
26 J.-M. Jin, D. Liu, W.-C. Chen, C. Shi, G. Chen, X. Wang, L. Xing, W. Ying, S. Ji, Y. Huo and S.-J. Su, *Angew. Chem., Int. Ed.*, 2024, **63**, e202401120.
27 X. Song, S. Shen, S. Zou, Y. Wang, F. Guo, S. Gao and Y. Zhang, *Chem. Eng. J.*, 2024, **481**, 148794.
28 W.-L. Tsai, M.-H. Huang, W.-K. Lee, Y.-J. Hsu, K.-C. Pan, Y.-H. Huang, H.-C. Ting, M. Sarma, Y.-Y. Ho, H.-C. Hu, C.-C. Chen, M.-T. Lee, K.-T. Wong and C.-C. Wu, *Chem. Commun.*, 2015, **51**, 13662–13665.
29 M. Y. Wong and E. Zysman-Colman, *Adv. Mater.*, 2017, **29**, 1605444.
30 Q. Zhang, B. Li, S. Huang, H. Nomura, H. Tanaka and C. Adachi, *Nat. Photonics*, 2014, **8**, 326–332.
31 J.-H. Jou, S. Kumar, A. Agrawal, T.-H. Li and S. Sahoo, *J. Mater. Chem. C*, 2015, **3**, 2974–3002.
32 P. L. dos Santos, J. S. Ward, M. R. Bryce and A. P. Monkman, *J. Phys. Chem. Lett.*, 2016, **7**, 3341–3346.
33 F. B. Dias, T. J. Penfold and A. P. Monkman, *Methods Appl. Fluoresc.*, 2017, **5**, 012001.
34 J. H. Kim, J. H. Yun and J. Y. Lee, *Adv. Opt. Mater.*, 2018, **6**, 1800255.
35 H.-Z. Li, F.-M. Xie, K. Zhang, Y. Shen, W. Zhou, Y.-Q. Li, W.-J. Wang and J.-X. Tang, *Chem. Eng. J.*, 2022, **436**, 135234.
36 R. Ma, Z. Ma, X. Wang, Z. Si, Q. Duan and S. Shao, *Chem. Eng. J.*, 2022, **447**, 137517.
37 X. Cai, J. Xue, C. Li, B. Liang, A. Ying, Y. Tan, S. Gong and Y. Wang, *Angew. Chem., Int. Ed.*, 2022, **61**, e202200337.
38 C.-Y. Chan, M. Tanaka, Y.-T. Lee, Y.-W. Wong, H. Nakanotani, T. Hatakeyama and C. Adachi, *Nat. Photonics*, 2021, **15**, 203–207.
39 J. Luo, S. Gong, Y. Gu, T. Chen, Y. Li, C. Zhong, G. Xie and C. Yang, *J. Mater. Chem. C*, 2016, **4**, 2442–2446.
40 K. Sun, X. Xie, Y. Liu, W. Jiang, X. Ban, B. Huang and Y. Sun, *J. Mater. Chem. C*, 2016, **4**, 8973–8979.
41 H. J. Kim, S. K. Kim, M. Godumala, J. Yoon, C. Y. Kim, J.-E. Jeong, H. Y. Woo, J. H. Kwon, M. J. Cho and D. H. Choi, *Chem. Commun.*, 2019, **55**, 9475–9478.
42 J. Duan, D. Liu, W. Tian, L. Jiang, W. Jiang and Y. Sun, *Opt. Mater.*, 2020, **104**, 109941.
43 X. Chen, S. Wang, H. L. Lee, J. Y. Lee, X. Liao, L. Li, W. Zhu and Y. Wang, *Adv. Opt. Mater.*, 2021, **9**, 2101518.
44 M. I. Alam, M. R. Nagar, S. R. Nayak, A. Choudhury, J.-H. Jou and S. Vaidyanathan, *Adv. Opt. Mater.*, 2022, **10**, 2200376.
45 Z. Fang, S. Wang, J. Liao, X. Chen, Y. Zhu, W. Zhu and Y. Wang, *J. Mater. Chem. C*, 2022, **10**, 4837–4844.
46 H.-H. Chou and C.-H. Cheng, *Adv. Mater.*, 2010, **22**, 2468–2471.
47 X. Yang, G. Zhou and W.-Y. Wong, *Chem. Soc. Rev.*, 2015, **44**, 8484–8575.
48 H. Noda, H. Nakanotani and C. Adachi, *Sci. Adv.*, 2018, **4**, eaao6910.
49 K. Li, Y. Zhu, B. Yao, Y. Chen, H. Deng, Q. Zhang, H. Zhan, Z. Xie and Y. Cheng, *Chem. Commun.*, 2020, **56**, 5957–5960.
50 W.-C. Chen, Z.-L. Zhu and C.-S. Lee, *Adv. Opt. Mater.*, 2018, **6**, 1800258.
51 P. Zassowski, P. Ledwon, A. Kurowska, A. P. Herman, M. Lapkowski, V. Cherpak, Z. Hotra, P. Turyk, K. Ivaniuk, P. Stakhira, G. Sych, D. Volyniuk and J. V. Grazulevicius, *Dyes Pigm.*, 2018, **149**, 804–811.
52 H. Lee, R. Braveenth, S. Muruganantham, C. Y. Jeon, H. S. Lee and J. H. Kwon, *Nat. Commun.*, 2023, **14**, 419.
53 X. Cai and S.-J. Su, *Adv. Funct. Mater.*, 2018, **28**, 1802558.
54 K. R. Naveen, P. Palanisamy, M. Y. Chae and J. H. Kwon, *Chem. Commun.*, 2023, **59**, 3685–3702.
55 B. Zhou, Z. Qi, M. Dai, C. Xing and D. Yan, *Angew. Chem., Int. Ed.*, 2023, **62**, e202309913.
56 X. Yang, G. I. N. Waterhouse, S. Lu and J. Yu, *Chem. Soc. Rev.*, 2023, **52**, 8005–8058.
57 J. U. Kim, I. S. Park, C.-Y. Chan, M. Tanaka, Y. Tsuchiya, H. Nakanotani and C. Adachi, *Nat. Commun.*, 2020, **11**, 1765.
58 Y. Xu, X. Liang, X. Zhou, P. Yuan, J. Zhou, C. Wang, B. Li, D. Hu, X. Qiao, X. Jiang, L. Liu, S.-J. Su, D. Ma and Y. Ma, *Adv. Mater.*, 2019, **31**, 1807388.
59 Y. Im, M. Kim, Y. J. Cho, J.-A. Seo, K. S. Yook and J. Y. Lee, *Chem. Mater.*, 2017, **29**, 1946–1963.

60 X. Cai, X. Li, G. Xie, Z. He, K. Gao, K. Liu, D. Chen, Y. Cao and S.-J. Su, *Chem. Sci.*, 2016, **7**, 4264–4275.
61 Y.-F. Sun, X.-L. Chen, D.-H. Zhang, P. Huo, Z. Liu, L. Zhou, F.-L. Lin and C.-Z. Lu, *Adv. Mater.*, 2024, **36**, 2408118.
62 Z. Li, Z. Chen, Z. Shi, G. Zou, L. Chu, X.-K. Chen, C. Zhang, S. K. So and H.-L. Yip, *Nat. Commun.*, 2023, **14**, 6441.
63 B. H. Jhun, Y. Park, H. S. Kim, J. H. Baek, J. Kim, E. Lee, H. Moon, C. Oh, Y. Jung, S. Choi, M.-H. Baik and Y. You, *Nat. Commun.*, 2025, **16**, 392.
64 M. Li, J. Jiang, Y. Ning, S. Zhao, W. F. A. Masri, S. Wageh and A. Al-Ghamdi, *Synth. Met.*, 2022, **289**, 117122.
65 G. Kreiza, D. Berenis, D. Banevičius, S. Juršėnas, T. Javorskis, E. Orentas and K. Kazlauskas, *Chem. Eng. J.*, 2021, **412**, 128574.
66 X. Zheng, R. Huang, C. Zhong, G. Xie, W. Ning, M. Huang, F. Ni, F. B. Dias and C. Yang, *Adv. Sci.*, 2020, **7**, 1902087.
67 Z. He, C. Wang, J. Zhao, X. Du, H. Yang, P. Zhong, C. Zheng, H. Lin, S. Tao and X. Zhang, *J. Mater. Chem. C*, 2019, **7**, 11806–11812.
68 X. Ban, F. Chen, J. Pan, Y. Liu, A. Zhu, W. Jiang and Y. Sun, *Chem. – Eur. J.*, 2020, **26**, 3090–3102.
69 B. Li, Z. Ding, Z. Wu, M. Liu, S. Chen, D. Chen, Z. Li, L. Sang, Y. Liu, L. Lin, W. Zhu and X. Wan, *Chem. Eng. J.*, 2023, **476**, 146484.
70 G. Liao, J. Lei, S. Li, M. Liu, Y. Qiao, K. Liu, N. Wang, Q. Niu and X. Yin, *Adv. Opt. Mater.*, 2024, **12**, 2301242.
71 X.-L. Chen, J.-H. Jia, R. Yu, J.-Z. Liao, M.-X. Yang and C.-Z. Lu, *Angew. Chem., Int. Ed.*, 2017, **56**, 15006–15009.
72 S. Wang, H. Zhang, B. Zhang, Z. Xie and W. Wong, *Mater. Sci. Eng., R*, 2020, **140**, 100547.
73 T. Huang, W. Jiang and L. Duan, *J. Mater. Chem. C*, 2018, **6**, 5577–5596.
74 Y. Zou, S. Gong, G. Xie and C. Yang, *Adv. Opt. Mater.*, 2018, **6**, 1800568.

